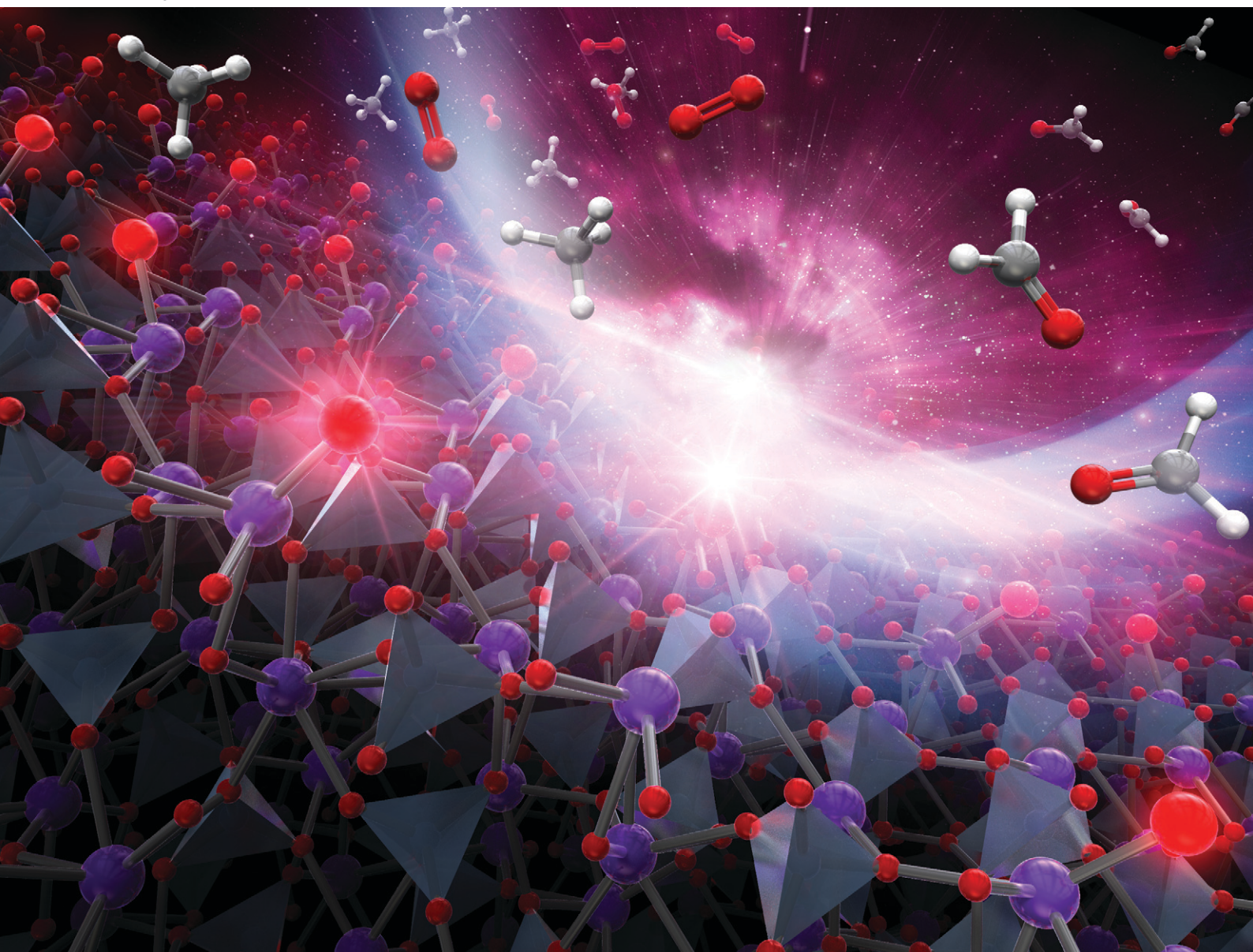


# Catalysis Science & Technology

Volume 13  
Number 18  
21 September 2023  
Pages 5143-5466

rsc.li/catalysis



ISSN 2044-4761

**PAPER**

Keigo Kamata *et al.*  
Bismuth phosphate nanoparticle catalyst for direct oxidation  
of methane into formaldehyde

Cite this: *Catal. Sci. Technol.*, 2023,  
13, 5180

# Bismuth phosphate nanoparticle catalyst for direct oxidation of methane into formaldehyde†

Aoi Matsuda,<sup>a</sup> Kazuhiko Obara,<sup>a</sup> Atsushi Ishikawa,<sup>b</sup> Meng-Hsuan Tsai,<sup>c</sup>  
Chia-Hsin Wang,<sup>c</sup> Yu-Chuan Lin,<sup>d</sup> Michikazu Hara<sup>a</sup> and Keigo Kamata<sup>\*a</sup>

The direct oxidation of methane (CH<sub>4</sub>) to formaldehyde (HCHO) with molecular oxygen (O<sub>2</sub>) as the sole oxidant was studied over various bismuth-based catalysts (BiPO<sub>4</sub>, α-Bi<sub>2</sub>O<sub>3</sub>, β-Bi<sub>2</sub>O<sub>3</sub>) using a fixed-bed flow reactor. The catalytic activity of monoclinic BiPO<sub>4</sub> nanoparticles (BiPO<sub>4</sub>-DEG) synthesized in a mixed solvent of diethylene glycol (DEG) and water for the direct oxidation of CH<sub>4</sub> was the highest among the catalysts tested. In high temperature region, BiPO<sub>4</sub>-DEG was more selective for HCHO formation than FePO<sub>4</sub> nanoparticles. Based on mechanistic studies including the catalyst effect, kinetics, pulse-reaction experiments, infrared (IR) spectroscopy, *operando* near ambient pressure X-ray photoelectron spectroscopy (NAP-XPS), and density functional theory (DFT) calculations, surface active oxygen species generated on BiPO<sub>4</sub> possibly react with CH<sub>4</sub> to give HCHO as the primary product. In contrast, the phosphate units of FePO<sub>4</sub> nanoparticles react with CH<sub>4</sub> followed by rapid reoxidation to FePO<sub>4</sub>.

Received 1st May 2023,  
Accepted 24th July 2023

DOI: 10.1039/d3cy00590a

rsc.li/catalysis

## 1. Introduction

Methane (CH<sub>4</sub>) has attracted attention as an important raw material due to its abundance around the world as a main component of natural gas and a low emitter of greenhouse gases such as carbon dioxide (CO<sub>2</sub>) compared to coal and oil.<sup>1</sup> However, CH<sub>4</sub> is mainly used as an energy source for heating, cooking, and power generation. The use of CH<sub>4</sub> as a chemical feedstock is very small due to the difficulty in activating the strong C–H bond (440 kJ mol<sup>-1</sup>).<sup>2</sup> Current CH<sub>4</sub> conversion into commodity chemicals and fuels is limited to indirect pathways *via* synthesis gas (CO + H<sub>2</sub>) produced by energy- and capital-intensive reforming processes.<sup>3</sup> Therefore, the development of catalytic processes that can directly convert CH<sub>4</sub> into useful chemicals and fuels is an important and challenging subjects, and various effective thermocatalytic,<sup>2,4–8</sup> electrocatalytic,<sup>9</sup> and plasma- or electric-field assisted systems<sup>10</sup> have been reported

for oxidative CH<sub>4</sub> upgrading and non-oxidative dehydrogenative aromatization.<sup>11,12</sup>

Various effective solid materials based on metal-exchanged zeolites,<sup>14–18</sup> metal oxides,<sup>19–22</sup> supported catalysts,<sup>23–25</sup> metal phosphates,<sup>26–36</sup> and metal organic frameworks<sup>37,38</sup> can function as efficient catalysts for oxidative upgrading of CH<sub>4</sub> such as oxidative coupling to ethylene (C<sub>2</sub>H<sub>4</sub>), oxygenation to methanol (CH<sub>3</sub>OH) and/or formaldehyde (HCHO), and oxidative halogenation using O<sub>2</sub>, H<sub>2</sub>O<sub>2</sub>, and N<sub>2</sub>O as oxidants. In particular, V- and Mo-based catalysts and B<sub>2</sub>O<sub>3</sub>/Al<sub>2</sub>O<sub>3</sub> are efficient catalysts for the oxidation of CH<sub>4</sub> into HCHO which is an important raw material as resins and polyfunctional alcohols.<sup>39–42</sup> The performance of V- and Mo-based catalysts is improved by the metal loading amounts and space velocity, and Cu–MoO<sub>x</sub> catalysts selectively give HCHO in 1.0% yield (62% select.) for the CH<sub>4</sub> oxidation at 700 °C in the presence of water vapor.<sup>41</sup> Non-metallic B<sub>2</sub>O<sub>3</sub>-based catalysts exhibit high HCHO yield and selectivity, and molecular O<sub>2</sub> bonded to tri-coordinated BO<sub>3</sub> centers on B<sub>2</sub>O<sub>3</sub> surfaces has been proposed as an active oxidant for CH<sub>4</sub> activation.<sup>42</sup>

Among the solid catalyst materials, we have also focused on metal phosphates with unique surface redox and acid–base properties for the direct oxidation of CH<sub>4</sub> with O<sub>2</sub> as the sole oxidant.<sup>28,43,44</sup> Monoclinic cerium orthophosphate (CePO<sub>4</sub>) nanorods efficiently catalyze the oxidative coupling of CH<sub>4</sub> in an electric field without the need for external heating.<sup>28,43</sup> Trigonal iron phosphate (FePO<sub>4</sub>) nanoparticles exhibits high activity for the selective oxidation of CH<sub>4</sub> into HCHO. The weakly-basic phosphate units likely contribute to

<sup>a</sup> Laboratory for Materials and Structures, Institute of Innovative Research, Tokyo Institute of Technology, 4259 Nagatsuta-cho, Midori-ku, Yokohama, Kanagawa 226-8503, Japan. E-mail: kamata.k.ac@m.titech.ac.jp

<sup>b</sup> Department of Transdisciplinary Science and Engineering, School of Environment and Society, Tokyo Institute of Technology, 2-12-1 Ookayama, Meguro-ku, Tokyo 152-8550, Japan

<sup>c</sup> National Synchrotron Radiation Research Center, 101 Hsin-Ann Rd., 30076, Hsinchu, Taiwan

<sup>d</sup> Department of Chemical Engineering, National Cheng Kung University, 1 University Rd., Tainan, 70101, Taiwan

† Electronic supplementary information (ESI) available. See DOI: <https://doi.org/10.1039/d3cy00590a>

the suppression of complete oxidation to  $\text{CO}_2$ .<sup>44</sup> While the redox-active Lewis acidic metal sites of metal phosphates play an important role in the activation of  $\text{CH}_4$  and  $\text{O}_2$ , the effect of metals and the reaction mechanism on the direct oxidation of  $\text{CH}_4$  is still unclear. Herein, we focus on bismuth, which is used as the main catalyst component in industrial propylene oxidation processes.<sup>45</sup> Although bismuth phosphates (Fig. 1) have been mostly investigated for photocatalytic reactions,<sup>46–51</sup> their application to other reactions (e.g., oxidative dehydrogenation,<sup>52–54</sup> ammoxidation,<sup>55</sup> decomposition,<sup>56</sup> isomerization,<sup>57</sup> aldol condensation<sup>58</sup>) including the direct oxidation of  $\text{CH}_4$  has not been sufficiently explored.<sup>23,26</sup>

In this paper, we report the selective oxidation of  $\text{CH}_4$  to  $\text{HCHO}$  with molecular oxygen ( $\text{O}_2$ ) as the sole oxidant over a  $\text{BiPO}_4$  catalyst using a fixed-bed flow reactor.  $\text{BiPO}_4$  nanoparticles ( $\text{BiPO}_4$ -DEG) synthesized in a mixed solvent in DEG/water exhibit higher catalytic activity and selectivity for  $\text{HCHO}$  than other bismuth-containing catalysts (Fig. 1) and  $\text{FePO}_4$  nanoparticles.<sup>44</sup> The mechanistic studies including the catalyst effect, pulse experiments, kinetics, operando analysis and density functional theory (DFT) calculations indicate that surface oxygen species generated on  $\text{BiPO}_4$  possibly react with  $\text{CH}_4$  to give  $\text{HCHO}$  as a primary product.

## 2. Experimental section

### 2.1. Instruments

X-ray diffraction (XRD), energy dispersive X-ray fluorescence spectroscopy (ED-XRF), Fourier transform infrared spectroscopy (FT-IR), thermogravimetry-differential thermal analysis (TG-DTA),  $\text{H}_2$  temperature-programmed reduction ( $\text{H}_2$ -TPR), nitrogen adsorption-desorption, scanning electron microscopy (SEM), transmission electron microscopy (TEM), and X-ray photoelectron spectroscopy (XPS) were performed using previously described instruments.<sup>44,59–61</sup> The details are described in the ESI.†

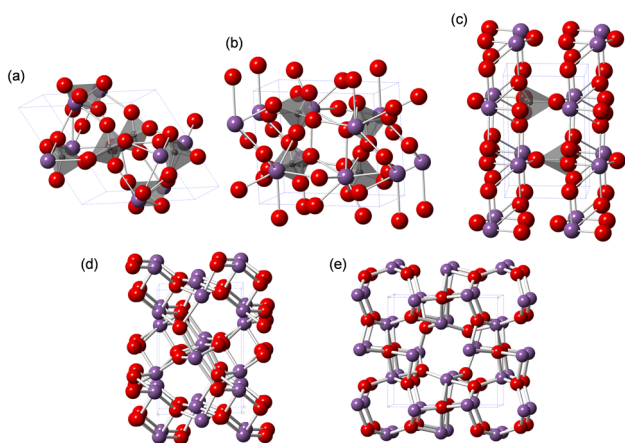


**Fig. 1** Structures of (a) trigonal  $\text{BiPO}_4 \cdot (\text{H}_2\text{O})_{0.67}$ , (b) monoclinic  $\text{BiPO}_4$  ( $P2_1/n$ ), and (c) monoclinic  $\text{BiPO}_4$  ( $P2_1/m$ ), (d) monoclinic  $\alpha\text{-Bi}_2\text{O}_3$ , and (e) tetragonal  $\beta\text{-Bi}_2\text{O}_3$ . Purple, gray, and red spheres represent Bi, P, and O atoms, respectively.

### 2.2. Synthesis of $\text{BiPO}_4$ -DEG

$\text{NH}_4\text{H}_2\text{PO}_4$  (1.035 g, 9 mmol) was dissolved in a mixed solution of diethylene glycol (DEG)/water (75 mL, 1/1 v/v). A DEG solution (30 mL) containing  $\text{Bi}(\text{NO}_3)_3 \cdot 5\text{H}_2\text{O}$  (4.37 g, 9 mmol) was added dropwise into this phosphate solution followed by stirring for 60 min at room temperature. The resulting precipitates were collected by centrifugation, washed with ethanol (40 mL  $\times$  3), and dried at 110 °C overnight to obtain  $\text{BiPO}_4 \cdot (\text{H}_2\text{O})_{0.67}$  as a precursor. This precursor was calcined at 600 °C for 5 h to give  $\text{BiPO}_4$ -DEG (2.54 g, 93% yield).

### 2.3. Synthesis of $\text{BiPO}_4$ -HT

$\text{BiPO}_4$ -HT was synthesized by a hydrothermal (HT) reaction.  $\text{Bi}(\text{NO}_3)_3 \cdot 5\text{H}_2\text{O}$  (6.00 mmol, 2.91 g) and  $(\text{NH}_4)_2\text{HPO}_4$  (6.00 mmol, 0.792 g) were added to water (70 mL) and stirred for 30 min at room temperature. The resulting solution was transferred into a stainless steel autoclave with a Teflon vessel liner (TAF-SR type, Taiatsu Techno Corporation). After the solution was heated at 180 °C for 18 h, the precipitates were collected by filtration and washed with water (200 mL). The resulting precipitates were calcined at 600 °C for 5 h and the  $\text{BiPO}_4$ -HT catalyst was obtained (1.75 g, 96% yield).

### 2.4. Catalytic oxidation of $\text{CH}_4$ with $\text{O}_2$

The oxidation of  $\text{CH}_4$  with  $\text{O}_2$  over various bismuth-based catalysts was conducted in a fixed-bed continuous-flow reactor operated at atmospheric pressure. All of the catalysts were pressed into pellets, crushed, and sieved to 32–42 meshes before the reaction. The catalyst (100 mg) was loaded into a quartz reactor (2 mm inner diameter at the catalyst bed portion) over a plug of quartz wool. When using a quartz reactor with larger inner diameter (4 mm) under the conditions in Fig. 3(d), the  $\text{HCHO}$  yield was not changed but the  $\text{CO}$  yield increased, which likely indicates quenching effect. A reaction gas containing  $\text{CH}_4/\text{O}_2/\text{N}_2$  in a molar ratio of 20/20/60 was used and the total gas flow rate was 10 sccm (i.e.,  $\text{CH}_4/\text{O}_2/\text{N}_2 = 2/2/6$  sccm). After introduction of the reaction gas flow to the reactor, the reaction temperature was increased from room temperature to 600 °C at a heating rate of ca. 40 °C  $\text{min}^{-1}$  and then held for 60 min. After the first sampling of the reaction gas, the temperature was decreased by 10 °C to 470 °C (420 °C in the case of  $\text{FePO}_4$ ) every 60 min with periodic analysis of the reaction gas. The products ( $\text{CO}$ ,  $\text{CO}_2$ ,  $\text{CH}_3\text{OH}$ ,  $\text{HCHO}$ ,  $\text{CH}_3\text{OCH}_3$ ,  $\text{C}_2\text{H}_6$ ,  $\text{C}_2\text{H}_4$ ) were analyzed using on-line gas chromatography (Shimadzu GC-8A) with a thermal conductivity detector (TCD) and two packed columns (a mixed column of Porapak-QS-N and molecular sieves 5A). All of the lines and valves between the reactor exit and the gas chromatograph were heated to 120–130 °C to prevent condensation of the products. Details of the calculations of  $\text{CH}_4$  conversion, yield, and selectivity are as follows:  $\text{CH}_4$  conversion (%) = carbon of ( $\text{CO}$ ,  $\text{CO}_2$ ,  $\text{HCHO}$ )/carbon of input  $\text{CH}_4 \times 100$ . Yield (%) = carbon of product/carbon of input  $\text{CH}_4 \times 100$ . Selectivity (%) = yield/ $\text{CH}_4$  conversion  $\times 100$ .

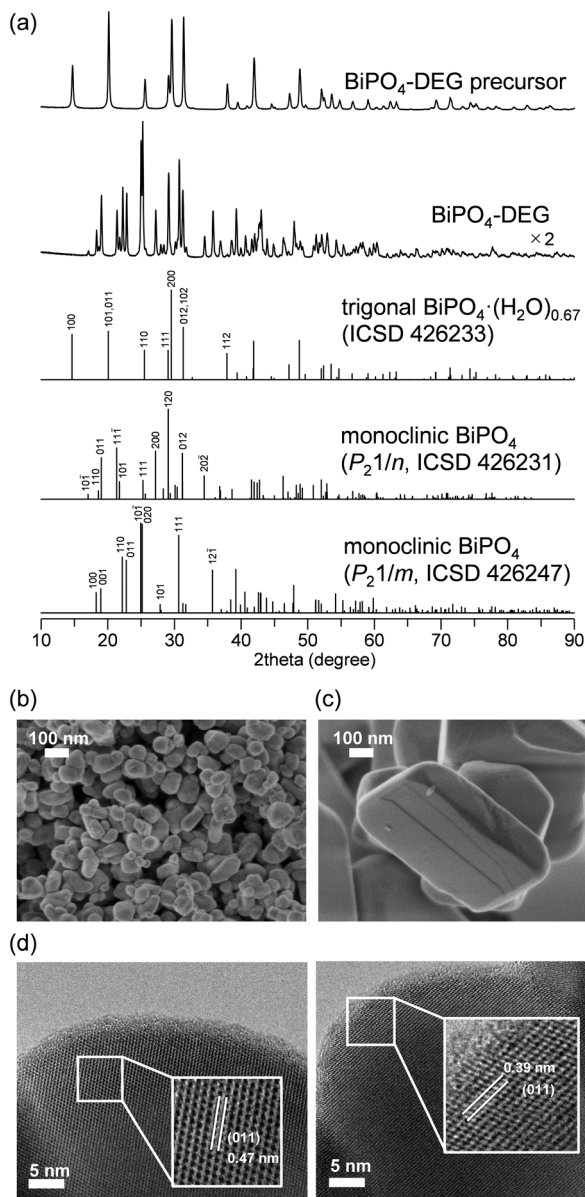


Fig. 2 (a) XRD patterns for BiPO<sub>4</sub>-DEG precursor, BiPO<sub>4</sub>-DEG, trigonal BiPO<sub>4</sub>·(H<sub>2</sub>O)<sub>0.67</sub> (ICSD 426233), monoclinic BiPO<sub>4</sub> (*P*<sub>2</sub>1/*n*, ICSD 426231), and monoclinic BiPO<sub>4</sub> (*P*<sub>2</sub>1/*m*, ICSD 426247). SEM images for (b) BiPO<sub>4</sub>-DEG and (c) BiPO<sub>4</sub>-HT. (d) TEM images for BiPO<sub>4</sub>-DEG.

Carbon balance (%) = (carbon of (CO, CO<sub>2</sub>, HCHO) + carbon of output CH<sub>4</sub>)/carbon of input CH<sub>4</sub> × 100. In each case, the carbon balance was in the range of 98.7 ± 1.4%.

### 2.5. Pulse-reaction experiments for CH<sub>4</sub> oxidation

The pulse-reaction experiments were performed using a quartz reactor (4 mm inner diameter at the catalyst bed portion) over a plug of quartz wool. The exit gas was directly connected to a gas chromatograph with a TCD (Shimadzu, GC-8A), and HCHO/CO<sub>2</sub> and CO were analyzed using Porapak-N and molecular sieves 5A columns, respectively. The details of the pulse-reactions of He-treated BiPO<sub>4</sub>-DEG

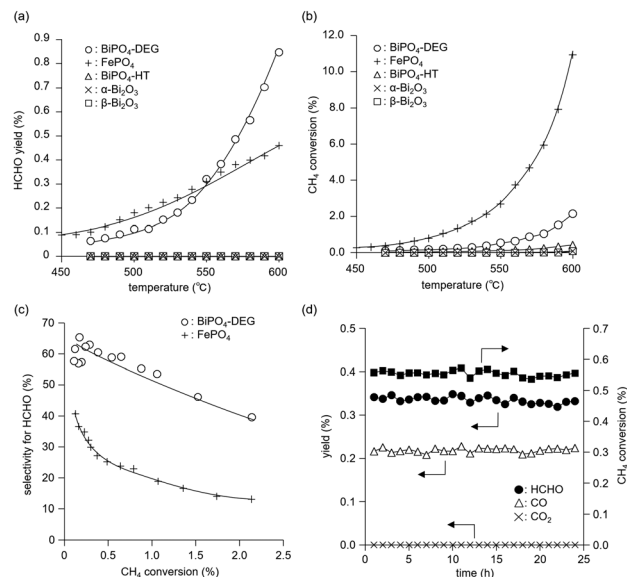


Fig. 3 (a) HCHO yield and (b) CH<sub>4</sub> conversion as a function of reaction temperature and (c) selectivity for HCHO as a function of CH<sub>4</sub> conversion over BiPO<sub>4</sub>-DEG, FePO<sub>4</sub>, BiPO<sub>4</sub>-HT,  $\alpha$ -Bi<sub>2</sub>O<sub>3</sub>, and  $\beta$ -Bi<sub>2</sub>O<sub>3</sub> catalysts. Reaction conditions: catalyst (100 mg), CH<sub>4</sub>/O<sub>2</sub>/N<sub>2</sub> (2/2/6 sccm), 420–600 °C. (d) Time-on-stream performance of BiPO<sub>4</sub>-DEG for oxidation of CH<sub>4</sub>. Reaction conditions: BiPO<sub>4</sub>-DEG (100 mg), CH<sub>4</sub>/O<sub>2</sub>/N<sub>2</sub> (2/2/6 sccm), 550 °C.

with (i) CH<sub>4</sub> or (ii) CH<sub>4</sub>/O<sub>2</sub> pulse are as follows. Prior to the pulse-reaction experiments, BiPO<sub>4</sub>-DEG (100 mg) was pretreated in a He flow (20 sccm) at 600 °C for 30 min followed by (i) CH<sub>4</sub> pulse (1 mL) or (ii) CH<sub>4</sub>/O<sub>2</sub> pulse (1 mL, 1/1 v/v) through the catalyst bed at 600 °C.

### 2.6. Computational details

The energy evaluation and geometry optimization of the atomic positions were carried out according to the following procedure. The initial atomic positions for the oxides were obtained from the experimental structure of monazite-type monoclinic BiPO<sub>4</sub> (*P*<sub>2</sub>1/*n*) taken from the inorganic crystal structure database (ICSD) with ID = 426 231. The unit cell consists of a 2 × 2 × 3 supercell, and the lower 2/3 of the unit cell was fixed during the geometry optimization. The core electrons were represented by the projector augmented-wave (PAW) method,<sup>62</sup> and the valence electrons were expanded by the plane wave basis set up to a cutoff energy of 400 eV. The meta-GGA SCAN functional was used as the exchange–correlation functional in the DFT calculations.<sup>63</sup> The Gaussian smearing method with  $\sigma = 0.1$  was used throughout for the smearing of the electron occupation near the Fermi level. The convergence thresholds for the electronic state calculation and geometry optimization were set to 1.0 × 10<sup>−5</sup> eV and 0.03 eV Å<sup>−1</sup> in energy and force, respectively. Integration in the reciprocal lattice space was performed by numerical integration using *k*-points, which were placed such that the spacing between them was 0.3 Å<sup>−1</sup>. The gamma point was always included. For isolated molecule calculations (H<sub>2</sub>,

O<sub>2</sub>, CH<sub>3</sub>, and CH<sub>4</sub>), a single *k*-point was placed on the gamma point. A vacuum layer with a thickness of 12 Å was placed between the slabs, and a dipole correction in the *z*-direction was introduced to remove the artificial interaction between slabs. All the calculations were performed with the Vienna *ab initio* simulation package (VASP) version 5.4.<sup>64,65</sup>

### 2.7. Operando near ambient pressure X-ray photoelectron spectroscopy (NAP-XPS) experiment

NAP-XPS analysis was performed at the Taiwan Light Source (TLS) beamline 24A of the National Synchrotron Radiation Research Center (NSRRC), Taiwan. The tested sample was pelleted and the spectra were recorded at 550 °C under evacuation and in O<sub>2</sub> atmosphere (0.1 mbar) in the NAP-XPS chamber. P 2p signal at 133.2 eV was used to correct the energy shift.

## 3. Results and discussion

### 3.1. Synthesis and characterization of bismuth phosphate nanoparticles

The low solubility of Bi species (*e.g.*, Bi(NO<sub>3</sub>)<sub>3</sub>) in aqueous media typically requires severe reaction conditions such as hydrothermal treatment to obtain bismuth phosphate (BiPO<sub>4</sub>) catalyst materials, which results in low specific surface areas. Thus, solvothermal and related synthesis methods are more effective for the synthesis of BiPO<sub>4</sub> nanoparticles. We also synthesized BiPO<sub>4</sub> nanoparticles (BiPO<sub>4</sub>-DEG) by the calcination of a precursor, which was prepared by the reaction of Bi(NO<sub>3</sub>)<sub>3</sub>·5H<sub>2</sub>O and NH<sub>4</sub>H<sub>2</sub>PO<sub>4</sub> in a mixed solution of diethylene glycol (DEG)/water, in air at 600 °C.

The XRD patterns for the precursor and BiPO<sub>4</sub>-DEG showed the formation of hydrated bismuth phosphate in the trigonal system (BiPO<sub>4</sub>·(H<sub>2</sub>O)<sub>0.67</sub>) and a mixture of monoclinic BiPO<sub>4</sub> (*P*<sub>2</sub>1/*n* and *P*<sub>2</sub>1/*m*), respectively (Fig. 2(a)). Braque and co-workers reported that the trigonal phase of BiPO<sub>4</sub>·(H<sub>2</sub>O)<sub>0.67</sub> (Fig. 1(a)) is metastable and irreversibly transforms to the monazite-type structure (*P*<sub>2</sub>1/*n*, Fig. 1(b)) and that this monazite-type BiPO<sub>4</sub> slowly transforms into the high-temperature monoclinic form (*P*<sub>2</sub>1/*m*, Fig. 1(c)) when heated above 600 °C.<sup>66</sup> No impurity phases such as bismuth phosphates, bismuth oxides, or phosphorous oxides were observed. Elemental analysis of BiPO<sub>4</sub>-DEG using energy dispersive X-ray fluorescence spectroscopy (ED-XRF) showed that the molar ratio of Bi/P was 1/1, which also supports the high purity. On the other hand, only the monazite-type structure was observed for BiPO<sub>4</sub>-HT synthesized by the hydrothermal reaction of Bi(NO<sub>3</sub>)<sub>3</sub> and (NH<sub>4</sub>)<sub>2</sub>HPO<sub>4</sub> at 180 °C followed by calcination at 600 °C in a similar manner to that of previous reports (Fig. S1†).<sup>47,49</sup>

The specific surface area of BiPO<sub>4</sub>-DEG was 10 m<sup>2</sup> g<sup>-1</sup>, which is much larger than that of BiPO<sub>4</sub>-HT (<1 m<sup>2</sup> g<sup>-1</sup>) (Table 1). SEM observations of BiPO<sub>4</sub>-DEG showed the formation of spherical nanoparticles with estimated particle sizes of *ca.* 50–100 nm (Fig. 2(b)), while large particles with sizes of hundreds of nanometers were observed for BiPO<sub>4</sub>-HT

**Table 1** Specific surface area, bulk content, and particle and crystallite size of the bismuth-based catalysts

Entry	Catalyst	<i>S</i> <sub>BET</sub> (m <sup>2</sup> g <sup>-1</sup> )	Crystallite size <sup>a</sup> (nm)
1	BiPO <sub>4</sub> -DEG precursor	14	38 (110)
2	BiPO <sub>4</sub> -DEG	10	<i>P</i> <sub>2</sub> 1/ <i>n</i> : 46 (10–1) <i>P</i> <sub>2</sub> 1/ <i>m</i> : 51 (12–1)
3	BiPO <sub>4</sub> -HT	<1	93 (10–1)
4	α-Bi <sub>2</sub> O <sub>3</sub>	1	97 (002)
5	β-Bi <sub>2</sub> O <sub>3</sub>	10	70 (201)
6 <sup>b</sup>	FePO <sub>4</sub>	22	33 (100) 22 (200)

<sup>a</sup> Calculated by the XRD peaks using Rigaku PDXL2 software. <sup>b</sup> Data from ref. 44.

(Fig. 2(c)). These nanoparticle sizes were in reasonable agreement with the grain sizes (*d* = 46 and 51 nm for BiPO<sub>4</sub> (*P*<sub>2</sub>1/*n* and *P*<sub>2</sub>1/*m*), respectively) calculated from the (10–1) and (12–1) diffraction lines, respectively, using Scherrer's equation. A similar morphology and size distribution of the nanoparticles were observed by TEM, with clear lattice fringes throughout the particles indicating their crystallinity (Fig. 2(d)). The distances between fringes of different particles were 0.47 and 0.39 nm, assigned to the *d*-spacing for the (011) planes of monazite-type (*P*<sub>2</sub>1/*n*) and high-temperature monoclinic BiPO<sub>4</sub> (*P*<sub>2</sub>1/*m*), respectively.<sup>47,50</sup>

### 3.2. Catalytic oxidation of CH<sub>4</sub> into HCHO with O<sub>2</sub>

The catalyst effect of bismuth-based materials (BiPO<sub>4</sub>-DEG, BiPO<sub>4</sub>-HT, α-Bi<sub>2</sub>O<sub>3</sub> (Fig. 1(d)), and β-Bi<sub>2</sub>O<sub>3</sub> (Fig. 1(e))) was investigated for the oxidation of CH<sub>4</sub> with O<sub>2</sub> as the sole oxidant. There were three main products, *i.e.*, such as formaldehyde (HCHO), carbon monoxide (CO), and carbon dioxide (CO<sub>2</sub>). Other products such as CH<sub>3</sub>OH were not observed (Fig. S2†). Fig. 3(a) shows the HCHO yield as a function of reaction temperature under a CH<sub>4</sub>/O<sub>2</sub>/N<sub>2</sub> (2/2/6 sccm) flow in the temperature range of 450–600 °C. BiPO<sub>4</sub>-DEG selectively gave HCHO with little formation of CO<sub>2</sub>. The formation of CO<sub>2</sub> was mainly observed using other bismuth-based catalysts such as BiPO<sub>4</sub>-HT, α-Bi<sub>2</sub>O<sub>3</sub>, and β-Bi<sub>2</sub>O<sub>3</sub> (Fig. 3(a) and S2†). There was no significant change in the XRD patterns for any of the Bi-based catalysts recovered after CH<sub>4</sub> oxidation (Fig. S3†), although some β-Bi<sub>2</sub>O<sub>3</sub> was changed to α-Bi<sub>2</sub>O<sub>3</sub>, which suggests that the catalytic performance is derived from their structures. Although the water vapor plays an important role in the oxidative conversion of CH<sub>4</sub> in some cases,<sup>67</sup> the presence of water vapor did not enhance the present CH<sub>4</sub> oxidation and HCHO yield/selectivity. The space time yield of BiPO<sub>4</sub>-DEG at 600 °C was 0.45 mmol<sub>HCHO</sub> g<sup>-1</sup> h<sup>-1</sup> (HCHO selectivity: 40%), and the value and selectivity for HCHO were higher than those for previously-reported Bi-based catalysts such as Bi<sub>2</sub>O<sub>3</sub>-B<sub>2</sub>O<sub>3</sub>/SiO<sub>2</sub> (4.3 × 10<sup>-2</sup> mmol<sub>HCHO</sub> g<sup>-1</sup> h<sup>-1</sup>, HCHO selectivity: 30%, 550 °C)<sup>23</sup> and Bi-P-O (7.7 × 10<sup>-2</sup> mmol<sub>HCHO</sub> g<sup>-1</sup> h<sup>-1</sup>, HCHO selectivity: 4%, 700 °C).<sup>26</sup>

Next, the catalytic performance of BiPO<sub>4</sub>-DEG was compared with that of FePO<sub>4</sub> nanoparticles, which are

effective heterogeneous catalysts for the direct oxidation of  $\text{CH}_4$  into HCHO.<sup>44</sup>  $\text{BiPO}_4$ -DEG functioned as a solid catalyst to efficiently give HCHO at high reaction temperatures compared to  $\text{FePO}_4$  (Fig. 3(a)). The HCHO yield of  $\text{BiPO}_4$ -DEG exceeded that of  $\text{FePO}_4$  above 550 °C, while  $\text{FePO}_4$  showed higher HCHO yield than  $\text{BiPO}_4$ -DEG below 550 °C. Notably, a significant difference in the selectivity for HCHO was observed between these two catalysts. Fig. 3(b) and (c) show the dependence of  $\text{CH}_4$  conversion on the reaction temperature and the relationship between selectivity to HCHO and  $\text{CH}_4$  conversion, respectively. In the case of  $\text{FePO}_4$ , the  $\text{CH}_4$  conversion increased up to ca. 10% at 600 °C and the selectivity for HCHO was ca. 15–40% in the range of ~2%  $\text{CH}_4$  conversion. On the other hand,  $\text{BiPO}_4$ -DEG showed ca. 40–70% selectivity for HCHO in the same  $\text{CH}_4$  conversion region, which suggests that  $\text{BiPO}_4$ -DEG more selectively promotes the direct oxidation of  $\text{CH}_4$  into HCHO than  $\text{FePO}_4$ .  $\text{BiPO}_4$ -DEG also exhibited durability without significant change in the selectivity for HCHO ( $60.6 \pm 1.6\%$ ) and CO ( $39.4 \pm 1.6\%$ ) and  $\text{CH}_4$  conversion ( $0.55 \pm 0.02\%$ ) at 550 °C for 24 h time-on-stream as shown in Fig. 3(d). On the other hand, the CO yield gradually decreased from 1.29% (1 h) to 0.52% (12 h) for the  $\text{CH}_4$  oxidation at 600 °C (Fig. S4(a)†), whereas the HCHO yield was not significantly changed for 12 h and  $\text{CO}_2$  was hardly formed in a similar way to the oxidation at 550 °C. Despite such a decrease in the CO yield, the HCHO yield and selectivity after 12 h were 0.74% and 59%, respectively, and higher than those of  $\text{FePO}_4$  (0.42% yield and 4% selectivity) at 600 °C. From the XRD pattern for the recovered  $\text{BiPO}_4$ -DEG catalyst after the reaction at 600 °C (Fig. S4(b)†), there was a structural change in the grain sizes for  $\text{BiPO}_4$ -DEG calculated from the diffraction lines using Scherrer's equation (from 46 to 82 nm for  $P_{21/n}$ ; from 51 to 56 nm for  $P_{21/m}$ ) and the ratio of  $P_{21/n}$  to  $P_{21/m}$  (from 50/50 to 20/80); thus, the bulk structures of  $\text{BiPO}_4$  gradually changed during the  $\text{CH}_4$  oxidation at 600 °C in sharp contrast to the reaction at 550 °C.

The temperature dependence of  $\text{CH}_4$  conversion and product selectivity in  $\text{CH}_4$  oxidation with  $\text{BiPO}_4$ -DEG is shown in Fig. 4(a). HCHO was selectively formed in the low-temperature region (~550 °C), and the  $\text{CH}_4$  conversion and selectivity for CO gradually increased with increasing reaction temperature. Fig. 4(b) shows the dependence of the  $\text{CH}_4$  conversion and selectivity for each product on the contact time ( $W/F_{\text{CH}_4}$ ). HCHO selectivity decreased with increasing  $W/F_{\text{CH}_4}$  but the  $\text{CH}_4$  conversion and CO selectivity increased, which suggests that HCHO is the primary product and CO is formed by sequential oxidation of HCHO. Such over-oxidation of HCHO into CO and  $\text{CO}_2$  is also observed in the direct oxidation of  $\text{CH}_4$  with  $\text{FePO}_4$ .<sup>44</sup>

### 3.3. Mechanistic studies on direct oxidation of $\text{CH}_4$ into HCHO over $\text{BiPO}_4$

We previously reported that not only the oxidizing ability of metal phosphates but also the surface acid–base properties

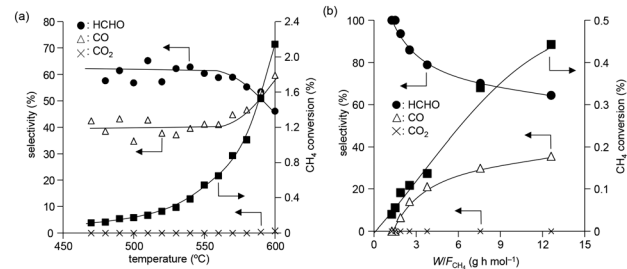


Fig. 4 (a) Product selectivity and  $\text{CH}_4$  conversion as function of reaction temperature with  $\text{O}_2$  over  $\text{BiPO}_4$ -DEG. Reaction conditions:  $\text{BiPO}_4$ -DEG (100 mg),  $\text{CH}_4/\text{O}_2/\text{N}_2$  (2/2/6 sccm). (b) Effect of  $W/F_{\text{CH}_4}$  on product selectivity and  $\text{CH}_4$  conversion. Reaction conditions:  $\text{BiPO}_4$ -DEG (100 mg),  $\text{CH}_4/\text{O}_2/\text{N}_2$  (38 : 8 : 54 molar ratio; total 7.8–78 sccm), reaction temperature (550 °C).

are key factors in the direct and selective oxidation of  $\text{CH}_4$ .<sup>28,43,44</sup> To investigate the oxidizing ability of Bi-based catalysts,  $\text{H}_2$ -temperature-programmed reduction ( $\text{H}_2$ -TPR) profiles were measured from 50 to 650 °C (Fig. 5). The reduction of  $\beta$ - $\text{Bi}_2\text{O}_3$  started around 250 °C, but the reduction of bismuth phosphates occurred at higher temperatures (from ~350 °C). The  $\text{H}_2$  consumption estimated from the  $\text{H}_2$ -TPR profiles below 550 °C decreased in the order of  $\beta$ - $\text{Bi}_2\text{O}_3$  ( $6.01 \text{ mmol g}^{-1}$ ) >  $\text{BiPO}_4$ -DEG ( $3.53 \text{ mmol g}^{-1}$ ) >  $\alpha$ - $\text{Bi}_2\text{O}_3$  ( $3.13 \text{ mmol g}^{-1}$ ) >  $\text{BiPO}_4$ -HT ( $1.03 \text{ mmol g}^{-1}$ ) >  $\text{FePO}_4$  ( $0.93 \text{ mmol g}^{-1}$ ),<sup>44</sup> which is significantly different from the order of  $\text{CH}_4$  conversion at 550 °C ( $\text{FePO}_4$  (2.69%) >  $\text{BiPO}_4$ -DEG (0.54%) >  $\text{BiPO}_4$ -HT (0.12%) >  $\alpha$ - $\text{Bi}_2\text{O}_3$  (<0.01%) >  $\beta$ - $\text{Bi}_2\text{O}_3$  (0%)) (Fig. S5†). In addition, the onset reduction temperature increased in the order of  $\beta$ - $\text{Bi}_2\text{O}_3$  (270 °C) <  $\text{BiPO}_4$ -DEG (320 °C) <  $\alpha$ - $\text{Bi}_2\text{O}_3$  (350 °C) <  $\text{FePO}_4$  (450 °C) <  $\text{BiPO}_4$ -HT (490 °C), and the order is also inconsistent with the order of reactivity for  $\text{CH}_4$  oxidation. A good correlation between  $\text{H}_2$  consumption and  $\text{CH}_4$  conversion has been reported in the case of iron-based phosphates and oxides.<sup>44</sup> Thus, the

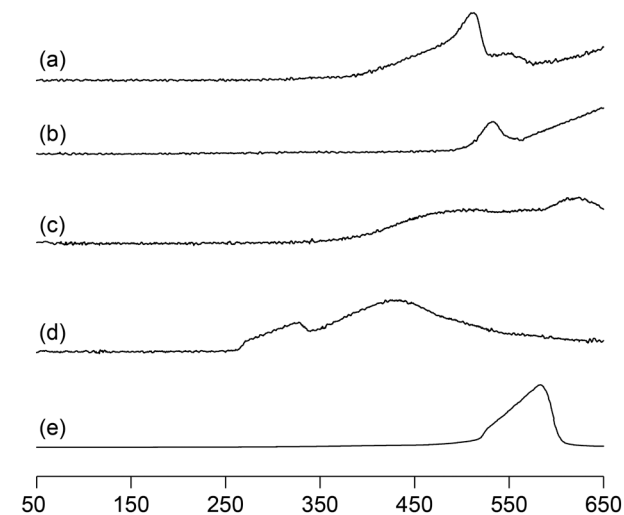


Fig. 5  $\text{H}_2$ -TPR profiles for (a)  $\text{BiPO}_4$ -DEG, (b)  $\text{BiPO}_4$ -HT, (c)  $\alpha$ - $\text{Bi}_2\text{O}_3$ , (d)  $\beta$ - $\text{Bi}_2\text{O}_3$ , and (e)  $\text{FePO}_4$ .

present discrepancy cannot be explained by the reaction mechanism in which lattice oxygen atoms of metal phosphates and oxides are involved in CH<sub>4</sub> oxidation.

Pulse-reaction experiments for BiPO<sub>4</sub>-DEG pretreated in He at 600 °C were conducted to determine the origin of the oxygen atoms incorporated in the oxygenated products (*i.e.*, from the oxygen atoms in BiPO<sub>4</sub> solid or the surface oxygen species generated from gaseous O<sub>2</sub>) (Table 2). No formation of oxygenated products was observed in the reaction of only the CH<sub>4</sub> pulse with BiPO<sub>4</sub>-DEG in sharp contrast to the FePO<sub>4</sub> nanoparticles that reacted with CH<sub>4</sub> to give C<sub>1</sub> products (HCHO and CO<sub>x</sub>) and partially reduced FePO<sub>4-δ</sub>.<sup>44</sup> On the other hand, HCHO, CO, and CO<sub>2</sub> were formed with selectivities of 44%, 54%, and 2%, respectively, at 0.9% CH<sub>4</sub> conversion when the CH<sub>4</sub> + O<sub>2</sub> pulse (1/1, v/v) was passed through the catalyst bed at 600 °C. The formation of C<sub>2</sub>-coupling products such as ethane and ethylene was not observed for both the pulse reaction and catalytic oxidation of CH<sub>4</sub> over BiPO<sub>4</sub>-DEG. Oxidative coupling of CH<sub>4</sub> (OCM) typically proceeds under the harsh reaction conditions (>650 °C) to cleave the strong C–H bonds of CH<sub>4</sub>, and it is well accepted that the generation of methyl radicals by the solid-catalyst surface with subsequent gas-phase propagation and termination is involved in the OCM mechanism.<sup>2,4,13</sup> These results suggest that the surface oxygen species generated from O<sub>2</sub> and BiPO<sub>4</sub> likely reacted with CH<sub>4</sub> to yield C<sub>1</sub> products (HCHO and CO<sub>x</sub>) without the formation of methyl radicals in the gas-phase. The kinetics of CH<sub>4</sub> oxidation over BiPO<sub>4</sub>-DEG at 550 °C were investigated. Fig. 6(a)–(c) show the dependence of the reaction rate (CH<sub>4</sub> conversion) on the partial pressures of CH<sub>4</sub> ( $P_{\text{CH}_4}$ ) and O<sub>2</sub> ( $P_{\text{O}_2}$ ), and the catalyst loading of BiPO<sub>4</sub>-DEG. A first-order dependence of the reaction rates on  $P_{\text{CH}_4}$  and catalyst loading was observed (Fig. 6(a) and (c)). The dependence of the reaction rate on  $P_{\text{O}_2}$  exhibited saturation kinetics (Fig. 6(b)), which is consistent with the Langmuir–Hinshelwood mechanism through adsorption (*i.e.*, activation) of O<sub>2</sub>.<sup>68–71</sup>

XPS measurements were performed to further investigate the surface structures of BiPO<sub>4</sub>-DEG. For the XPS Bi 4f spectrum of BiPO<sub>4</sub>-DEG at room temperature, a main peak around 159.8 eV (Bi 4f<sub>7/2</sub>) assignable to Bi<sup>3+</sup> species in BiPO<sub>4</sub> and a slight peak around 155.9 eV of metallic Bi species were observed (Fig. 7(a)).<sup>72,73</sup> Such formation of metallic Bi species has also been reported for BiPO<sub>4</sub> synthesized in ethylene glycol solvent probably due to the weak reducing ability of

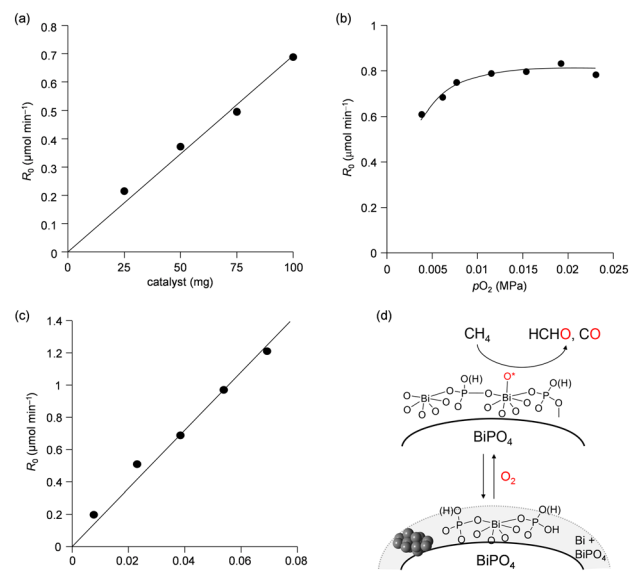


Fig. 6 Effect of (a) catalyst amount and partial pressure of (b) O<sub>2</sub> and (c) CH<sub>4</sub> on reaction rate. Reaction conditions for (a): BiPO<sub>4</sub>-DEG (25–100 mg), CH<sub>4</sub>/O<sub>2</sub>/N<sub>2</sub> (5/1/7 sccm; total 13 sccm), reaction temperature (550 °C). Reaction conditions for (b): BiPO<sub>4</sub>-DEG (100 mg), CH<sub>4</sub>/O<sub>2</sub>/N<sub>2</sub> (5/0.5–3/7.5–5 sccm; total 13 sccm), reaction temperature (550 °C). Reaction conditions for (c): BiPO<sub>4</sub>-DEG (100 mg), CH<sub>4</sub>/O<sub>2</sub>/N<sub>2</sub> (1–9/1/11–3 sccm; total 13 sccm), reaction temperature (550 °C). (d) Proposed reaction mechanism for oxidation of CH<sub>4</sub> with O<sub>2</sub> over BiPO<sub>4</sub>-DEG.

ethylene glycol.<sup>48</sup> It has also been reported that the formation of surface oxygen vacancies of BiPO<sub>4</sub> leads to the disordered edge of BiPO<sub>4</sub> particles observed by TEM analyses.<sup>51</sup> In the case of BiPO<sub>4</sub>-DEG, the edge of the nanoparticles become disordered (thickness ~1 nm, Fig. 2(d)), which supports the formation of metallic Bi species. The XPS O 1s spectrum of

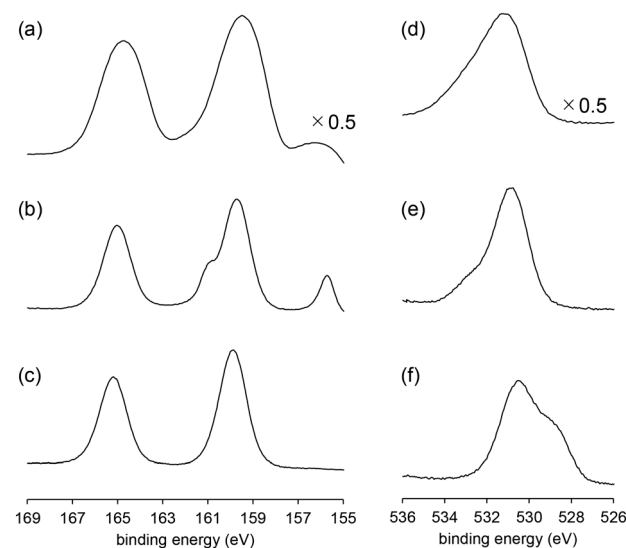


Fig. 7 XPS (a–c) Bi 4f and (d–f) O 1s spectra of BiPO<sub>4</sub>-DEG. (a and d) BiPO<sub>4</sub>-DEG at room temperature under evacuation, (b and e) BiPO<sub>4</sub>-DEG at 550 °C under evacuation, and (c and f) BiPO<sub>4</sub>-DEG at 550 °C under O<sub>2</sub> (0.1 mbar).

Table 2 Pulse reaction experiments on oxidation of CH<sub>4</sub> with BiPO<sub>4</sub>-DEG<sup>a</sup>

Entry	Pulse	CH <sub>4</sub> conversion (%)	Yield (%) (selectivity (%))		
			HCHO	CO	CO <sub>2</sub>
1	CH <sub>4</sub>	<0.01	<0.01 (—)	<0.01 (—)	<0.01 (—)
2	CH <sub>4</sub> + O <sub>2</sub> (1/1, v/v)	0.93	0.41 (44)	0.50 (54)	0.02 (2)

<sup>a</sup> Reaction conditions: BiPO<sub>4</sub>-DEG (100 mg), He (20 sccm), pulse volume (1 mL), reaction temperature (600 °C).

BiPO<sub>4</sub>-DEG also showed a peak around 533 eV which corresponds to adsorbed water in addition to the main peak around 531 eV assignable to lattice oxygen of BiPO<sub>4</sub>.

Surface oxygen species are formed on a CePO<sub>4</sub> catalyst through the activation of the O<sub>2</sub> molecule assisted by the electric field. Such active oxygen species possibly facilitate the oxidative coupling of the CH<sub>4</sub> reaction even at low temperature. In this case, the surface Lewis acidic Ce sites would play an important role in the activation of O<sub>2</sub>.<sup>28,43</sup> Therefore, the surface acid properties of the present BiPO<sub>4</sub>-DEG catalyst were investigated by IR measurements of samples adsorbed with pyridine and acetone. The IR spectrum for pyridine-adsorbed BiPO<sub>4</sub>-DEG showed a band at 1446 cm<sup>-1</sup> assignable to the pyridine species coordinated to the Lewis acid sites, and no band at 1540 cm<sup>-1</sup> due to pyridinium ions bonded to the Brønsted acid sites (Fig. 8(a)). The amount of Lewis acid sites was estimated to be 26 μmol g<sup>-1</sup> from the intensity of the band at 1446 cm<sup>-1</sup>. The density of surface Bi cations on BiPO<sub>4</sub>-DEG was calculated to be 1.6 nm<sup>-2</sup> from the BET surface area of BiPO<sub>4</sub>-DEG and the amounts of Lewis acid sites measured using pyridine-adsorbed IR. This value was comparable to that for monoclinic CePO<sub>4</sub> nanorods (1.6 nm<sup>-2</sup>) with monazite-type structure and the calculated value estimated from the main surface structure obtained from HAADF-STEM observation.<sup>28,29</sup> The IR spectrum of acetone adsorbed on BiPO<sub>4</sub>-DEG (Fig. 8(b)) showed one strong C=O stretching band due to acetone molecules coordinated to Lewis acid sites, with the band position at a lower wavenumber (1683 cm<sup>-1</sup>) than those for acetone in the gas phase (1731 cm<sup>-1</sup>), CePO<sub>4</sub> (1699 cm<sup>-1</sup>), and FePO<sub>4</sub> (1685 cm<sup>-1</sup>).<sup>28,43,44</sup> All these results support the presence of uniform surface Lewis acidic Bi species on the BiPO<sub>4</sub>-DEG nanoparticles. Such coordinatively unsaturated sites would be involved in the O<sub>2</sub> activation. In addition, the basicity was also evaluated by IR spectroscopy with adsorbed CHCl<sub>3</sub> and CH<sub>3</sub>OH (Fig. 8(c) and (d)). The presence of weakly-basic phosphate units on BiPO<sub>4</sub> was confirmed,<sup>‡</sup> which likely contributes to

the suppression of complete oxidation to CO<sub>2</sub> in a similar way to the CH<sub>4</sub> oxidation over FePO<sub>4</sub>.<sup>44</sup>

To obtain information on possible active oxygen species formed on surface Bi sites, an *operando* near-ambient-pressure X-ray photoelectron spectroscopy (NAP-XPS) experiment was conducted under O<sub>2</sub> atmosphere. When BiPO<sub>4</sub>-DEG was exposed to O<sub>2</sub> (0.1 mbar) at 550 °C, only the peak corresponding to BiPO<sub>4</sub> was observed in the XPS Bi 4f spectra with the disappearance of the peak of metallic Bi, which suggests reconstruction of the surface structure. The XPS O 1s spectra also changed during the reaction of BiPO<sub>4</sub>-DEG with O<sub>2</sub>. While the main peak around 531 eV assignable to lattice oxygens of BiPO<sub>4</sub> was unchanged, the peak around 533 eV corresponding to adsorbed oxygen atoms disappeared and a new peak around 529 eV appeared upon exposure of O<sub>2</sub>. It has been reported that the peaks due to bismuth oxides are in the range of 528.8–529.9 eV and that the negative shift of O 1s peaks is likely caused by the presence of non-bridging Bi–O species.<sup>74–78</sup> Thus, the new peak may be caused by surface oxygen species such as Bi–O species generated on BiPO<sub>4</sub>, which possibly react with CH<sub>4</sub> to give HCHO as a primary product. There was no significant difference in the XPS Bi 4f spectra between the fresh and recovered BiPO<sub>4</sub>-DEG catalysts after the CH<sub>4</sub> oxidation under the conditions in Fig. S6,† which suggests that the *in situ* generated oxygen species observed in the reaction temperature range play an important role in the present CH<sub>4</sub> oxidation.

To further investigate possible involvement of surface active oxygen species on BiPO<sub>4</sub>, density functional theory (DFT) calculations were carried out. Since the surface Bi density of BiPO<sub>4</sub>-DEG was comparable to that of monoclinic CePO<sub>4</sub> nanorods as described above, the monazite-type structure (P<sub>2</sub>1/n) was used as a model catalyst for the CH<sub>4</sub> oxidation. Surface energy calculations for the (100), (110), and (111) surfaces of BiPO<sub>4</sub> identified that the (100) surface is the most stable one. Furthermore, the DFT-based thermodynamic analysis have shown that the partially oxidized BiPO<sub>4</sub> (100) surface (0.25 monolayer) in which O atom adsorbed on Bi is the stable surface under the reaction environment (see the details in ESI,† Fig. S7 and S8). The following two pathways the CH<sub>4</sub> activation were compared: (i) H-abstraction by surface O atom and CH<sub>3</sub> adsorption on PO<sub>4</sub> units, and (ii) H-abstraction by lattice O atom and CH<sub>3</sub> adsorption on PO<sub>4</sub> units. Fig. 9 shows the optimized geometry and the reaction energies for CH<sub>4</sub> activation by these two pathways. The reaction energy (ΔE) is

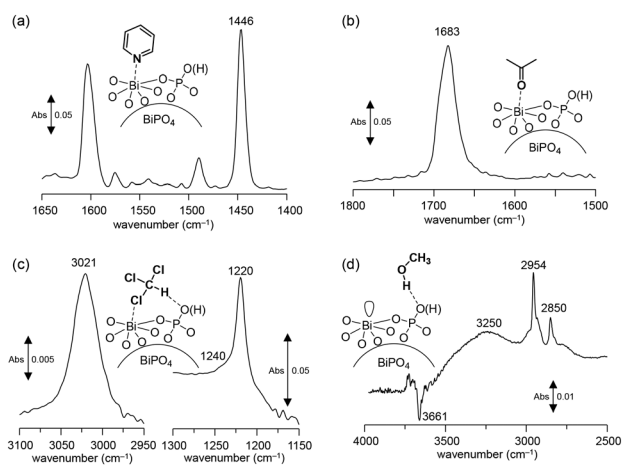
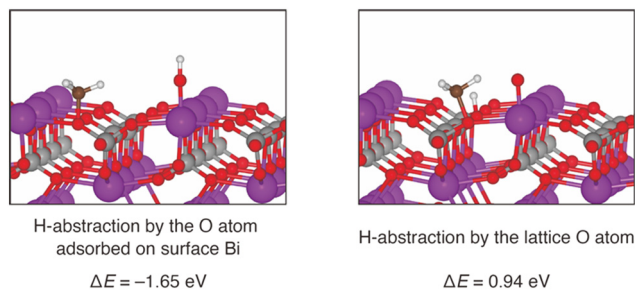


Fig. 8 Difference IR spectra for (a) pyridine-, (b) acetone-, (c) chloroform-, and (d) CH<sub>3</sub>OH-adsorbed BiPO<sub>4</sub>-DEG at 25 °C.

‡ The basicity was confirmed by IR spectroscopy with adsorbed CHCl<sub>3</sub> (Fig. 8(c) and (d)). The red-shift of the original C–H stretching mode of the CHCl<sub>3</sub> molecule from 3034 cm<sup>-1</sup> to 3021 cm<sup>-1</sup> indicates the presence of basic sites on the surface.<sup>74</sup> The band shift (13 cm<sup>-1</sup>) was larger than that for FePO<sub>4</sub> (~1 cm<sup>-1</sup>) but lower than that for CePO<sub>4</sub> (26 cm<sup>-1</sup>); thus, the basicity of BiPO<sub>4</sub> was stronger than that of FePO<sub>4</sub> but weaker than that of CePO<sub>4</sub>.<sup>39,40</sup> In the IR spectrum of BiPO<sub>4</sub>-DEG with adsorbed CH<sub>3</sub>OH, broad bands between 3000 and 3500 cm<sup>-1</sup> appeared with negative ν(O–H) bands, and bands at 2954 and 2850 cm<sup>-1</sup> assignable to the asymmetric and symmetric CH<sub>3</sub> stretching modes of molecularly adsorbed CH<sub>3</sub>OH, respectively, were observed. All these results are consistent with previous reports for the interaction of probe molecules on metal phosphates with uniform Lewis acid sites and weak base sites.





**Fig. 9** Optimized structure of the product state of the  $\text{CH}_4$  activation on 0.25 ML Bi-oxidized  $\text{BiPO}_4$  (100) surface. Two reaction pathways are considered, and their reaction energies ( $\Delta E$ s) calculated with the DFT are shown.

defined as the dissociative adsorption energy of  $\text{CH}_4$ . H-abstraction using a surface O atom is an exothermic reaction, since the calculated  $\Delta E$  is  $-1.65$  eV. On the other hand, H-abstraction by a lattice O atom is an endothermic reaction ( $\Delta E = 0.94$  eV). Thus, our calculations indicate that the  $\text{CH}_4$  activation takes place using surface O atoms, and not lattice O atoms. The surface O atoms are formed from gaseous  $\text{O}_2$  in the inlet gas, and therefore  $\text{CH}_4$  activation requires the presence of  $\text{O}_2$ . This is consistent with the observed reaction rate dependence on  $P_{\text{O}_2}$ , as seen in Fig. 6. In addition to the possible involvement of surface oxygen species generated on  $\text{BiPO}_4$ , the weak basicity on  $\text{BiPO}_4$  (Fig. 8(c) and (d)),<sup>‡</sup> similar to those on  $\text{FePO}_4$  and  $\text{CePO}_4$ , likely leads to high HCHO selectivity of  $\text{BiPO}_4$ -DEG.<sup>79</sup>

## Conclusions

In summary, bismuth-based phosphate and oxide catalysts were investigated for the oxidation of  $\text{CH}_4$  with  $\text{O}_2$  as the sole oxidant. Monoclinic  $\text{BiPO}_4$  nanoparticles ( $\text{BiPO}_4$ -DEG) exhibited higher catalytic performance for the direct oxidation of  $\text{CH}_4$  into HCHO than  $\text{BiPO}_4$  synthesized by the hydrothermal method ( $\text{BiPO}_4$ -HT),  $\alpha$ - $\text{Bi}_2\text{O}_3$ , and  $\beta$ - $\text{Bi}_2\text{O}_3$ . The lack of correlation between the catalytic activity and oxidizing ability estimated by  $\text{H}_2$ -TPR and pulse reaction experiments suggested that  $\text{CH}_4$  oxidation did not proceed with lattice oxygen supplied from the  $\text{BiPO}_4$ -DEG solid. On the basis of mechanistic studies including the catalyst effect, kinetics, NAP-XPS, and DFT calculations, the oxidation of  $\text{CH}_4$  may proceed at surface oxygen species generated on surface Bi atoms of  $\text{BiPO}_4$ . IR spectroscopy measurements of  $\text{BiPO}_4$ -DEG with adsorbed probe molecules indicate the presence of uniform Lewis acid sites and weak basic sites, which possibly activate  $\text{O}_2$  and suppress subsequent oxidation into  $\text{CO}_2$ , respectively. Such a possible  $\text{O}_2$  activation mode for  $\text{BiPO}_4$ -DEG would result in high selective formation of HCHO at high temperatures in sharp contrast to  $\text{FePO}_4$  nanoparticles with the redox mechanism.

## Author contributions

A. M. and K. O. designed the experiments, performed the experimental investigation, and conducted data analyses with

the help of K. K. A. I. performed the DFT calculations. M. T., C. W., Y. L. performed the NAP-XPS analyses. K. K., A. I., and Y. L. wrote the paper. The draft was reviewed by A. M., A. I., Y. L., M. H. and K. K.

## Conflicts of interest

There are no conflicts to declare.

## Acknowledgements

This study was funded in part by a Grant-in-Aid (21H01713) for Scientific Research from the Japan Society for the Promotion of Science (JSPS), and the PRESTO (JPMJPR15S3 and JPMJPR17S1), CREST (JPMJCR16P3), and A-STEP (JPMJTR20TG) programs of the Japan Science and Technology Agency (JST), and the “Design and Engineering by Joint Inverse Innovation for Materials Architecture” program of the Japan Ministry of Education, Culture, Sports, Science and Technology (MEXT).

## Notes and references

- 1 D. Saha, H. A. Grappe, A. Chakraborty and G. Orkoulas, *Chem. Rev.*, 2016, **116**, 11436–11499.
- 2 R. Horn and R. Schlögl, *Catal. Lett.*, 2015, **145**, 23–39.
- 3 A. Abdulrasheed, A. A. Jalil, Y. Gambo, M. Ibrahim, H. U. Hambali and M. Y. Shahul Hamid, *Renewable Sustainable Energy Rev.*, 2019, **108**, 175–193.
- 4 C. Hammond, S. Conrad and I. Hermans, *ChemSusChem*, 2012, **5**, 1668–1686.
- 5 K. Otsuka and Y. Wang, *Appl. Catal., A*, 2001, **222**, 145–161.
- 6 A. I. Olivos-Suarez, À. Szécsényi, E. J. M. Hensen, J. Ruiz-Martinez, E. A. Pidko and J. Gascon, *ACS Catal.*, 2016, **6**, 2965–2981.
- 7 M. Ravi, M. Ranocchiari and J. A. van Bokhoven, *Angew. Chem., Int. Ed.*, 2017, **56**, 16464–16483.
- 8 A. V. Vekki and S. T. Marakaev, *Russ. J. Appl. Chem.*, 2009, **82**, 521–536.
- 9 A. H. Bagherzadeh Mostaghimi, T. A. Al-Attas, M. G. Kibria and S. Siahrostami, *J. Mater. Chem. A*, 2020, **8**, 15575–15590.
- 10 S. Ogo and Y. Sekine, *Chem. Rec.*, 2017, **17**, 726–738.
- 11 I. Vollmer, I. Yarulina, F. Kapteijn and J. Gascon, *ChemCatChem*, 2018, **11**, 39–52.
- 12 K. Sun, D. M. Ginosar, T. He, Y. Zhang, M. Fan and R. Chen, *Ind. Eng. Chem. Res.*, 2018, **57**, 1768–1789.
- 13 H. Schwarz, *Angew. Chem., Int. Ed.*, 2011, **50**, 10096–10115.
- 14 M. H. Mahyuddin, Y. Shiota and K. Yoshizawa, *Catal. Sci. Technol.*, 2019, **9**, 1744–1768.
- 15 Z. Jin, L. Wang, E. Zuidema, K. Mondal, M. Zhang, J. Zhang, C. Wang, X. Meng, H. Yang, C. Mesters and F.-S. Xiao, *Science*, 2020, **367**, 193–197.
- 16 P. Xiao, Y. Wang, T. Nishitoba, J. N. Kondo and T. Yokoi, *Chem. Commun.*, 2019, **55**, 2896–2899.
- 17 C. Hammond, M. M. Forde, M. H. Ab Rahim, A. Thetford, Q. He, R. L. Jenkins, N. Dimitratos, J. A. Lopez-Sanchez, N. F. Dummer, D. M. Murphy, A. F. Carley, S. H. Taylor, D. J.

- Willock, E. E. Stangland, J. Kang, H. Hagen, C. J. Kiely and G. J. Hutchings, *Angew. Chem., Int. Ed.*, 2012, **51**, 5129–5133.
- 18 B. E. R. Snyder, M. L. Bols, R. A. Schoonheydt, B. F. Sels and E. I. Solomon, *Chem. Rev.*, 2018, **118**, 2718–2768.
- 19 P. Schwach, M. G. Willinger, A. Trunschke and R. Schlögl, *Angew. Chem., Int. Ed.*, 2013, **52**, 11381–11384.
- 20 J. H. Lunsford, *Angew. Chem., Int. Ed. Engl.*, 1995, **34**, 970–980.
- 21 B. P. C. Hereijgers and B. M. Weckhuysen, *ChemSusChem*, 2009, **2**, 743–748.
- 22 M. Bugnola, R. Carmieli and R. Neumann, *ACS Catal.*, 2018, **8**, 3232–3236.
- 23 K. Otsuka and M. Hatano, *J. Catal.*, 1987, **108**, 252–255.
- 24 K. Harrath, X. Yu, H. Xiao and J. Li, *ACS Catal.*, 2019, **9**, 8903–8909.
- 25 C. Williams, J. H. Carter, N. F. Dummer, Y. K. Chow, D. J. Morgan, S. Yacob, P. Serna, D. J. Willock, R. J. Meyer, S. H. Taylor and G. J. Hutchings, *ACS Catal.*, 2018, **8**, 2567–2576.
- 26 T. Ohno and J. B. Moffat, *Catal. Lett.*, 1992, **16**, 181–190.
- 27 A. V. Annapragada and E. Gulari, *J. Catal.*, 1990, **123**, 130–146.
- 28 A. Sato, S. Ogo, K. Kamata, Y. Takeno, T. Yabe, T. Yamamoto, S. Matsumura, M. Hara and Y. Sekine, *Chem. Commun.*, 2019, **55**, 4019–4022.
- 29 V. Paunović, G. Zichittella, M. Moser, A. P. Amrute and J. Pérez-Ramírez, *Nat. Chem.*, 2016, **8**, 803–809.
- 30 G. Zichittella, V. Paunović, A. P. Amrute and J. Pérez-Ramírez, *ACS Catal.*, 2017, **7**, 1805–1817.
- 31 Y. Wang and K. Otsuka, *J. Catal.*, 1995, **155**, 256–267.
- 32 Y. Wang, X. Wang, Z. Su, Q. Guo, Q. Tang, Q. Zhang and H. Wan, *Catal. Today*, 2004, **93–95**, 155–161.
- 33 G. O. Alptekin, A. M. Herring, D. L. Williamson, T. R. Ohno and R. L. McCormick, *J. Catal.*, 1999, **181**, 104–112.
- 34 Y. Wang and K. Otsuka, *J. Mol. Catal. A: Chem.*, 1996, **111**, 341–356.
- 35 Y. Wang and K. Otsuka, *J. Chem. Soc., Faraday Trans.*, 1995, **91**, 3953–3961.
- 36 V. Gomonaj and H. Toulhoat, *ACS Catal.*, 2018, **8**, 8263–8272.
- 37 J. Baek, B. Rungtaweeworanit, X. Pei, M. Park, S. C. Fakra, Y.-S. Liu, R. Matheu, S. A. Alshimri, S. Alshehri, C. A. Trickett, G. A. Somorjai and O. M. Yaghi, *J. Am. Chem. Soc.*, 2018, **140**, 18208–18216.
- 38 T. Ikuno, J. Zheng, A. Vjunov, M. Sanchez-Sanchez, M. A. Ortuno, D. R. Pahls, J. L. Fulton, D. M. Camaioni, Z. Li, D. Ray, B. L. Mehdi, N. D. Browning, O. K. Farha, J. T. Hupp, C. J. Cramer, L. Gagliardi and J. A. Lercher, *J. Am. Chem. Soc.*, 2017, **139**, 10294–10301.
- 39 V. Fornés, C. López, H. H. López and A. Martínez, *Appl. Catal., A*, 2003, **249**, 345–354.
- 40 H. Launay, S. Loricant, A. Pigamo, J. L. Dubois and J. M. M. Millet, *J. Catal.*, 2007, **246**, 390–398.
- 41 T. Akiyama, R. Sei and S. Takenaka, *Catal. Sci. Technol.*, 2021, **11**, 5273–5281.
- 42 J. Tian, J. Tan, Z. Zhang, P. Han, M. Yin, S. Wan, J. Lin, S. Wang and Y. Wang, *Nat. Commun.*, 2020, **11**, 5693.
- 43 S. Kanai, I. Nagahara, Y. Kita, K. Kamata and M. Hara, *Chem. Sci.*, 2017, **8**, 3146–3153.
- 44 A. Matsuda, H. Tateno, K. Kamata and M. Hara, *Catal. Sci. Technol.*, 2021, **11**, 6987–6998.
- 45 P. Sprenger, W. Kleist and J.-D. Grunwaldt, *ACS Catal.*, 2017, **7**, 5628–5642.
- 46 W. K. Darkwah, B. B. Adormaa, M. K. C. Sandrine and Y. Ao, *Catal. Sci. Technol.*, 2019, **9**, 546–566.
- 47 C. Pan, J. Xu, Y. Chen and Y. Zhu, *Appl. Catal., B*, 2012, **115–116**, 314–319.
- 48 F. Tian, H. Zhao, G. Li, Z. Dai, Y. Liu and R. Chen, *ChemSusChem*, 2016, **9**, 1579–1585.
- 49 J. Xu, L. Li, C. Guo, Y. Zhang and W. Meng, *Appl. Catal., B*, 2013, **130–131**, 285–292.
- 50 Y. Guo, P. Wang, J. Qian, Y. Ao, C. Wang and J. Hou, *Appl. Catal., B*, 2018, **234**, 90–99.
- 51 Y. Lv, Y. Zhu and Y. Zhu, *J. Phys. Chem. C*, 2013, **117**, 18520–18528.
- 52 F. Qiu, L. T. Weng, P. Ruiz and B. Delmon, *Appl. Catal.*, 1989, **47**, 115–123.
- 53 N. Abadzhjieva, P. Tzokov, I. Uzunov, V. Minkov, D. Klissurski and V. Rives, *React. Kinet. Catal. Lett.*, 1994, **53**, 413–418.
- 54 M. Ruwet, S. Ceckiewicz and B. Delmon, *Ind. Eng. Chem. Res.*, 1987, **26**, 1981–1983.
- 55 T.-S. Chang, L. Gujia, C.-H. Shin, Y. K. Lee and S.-S. Yun, *Catal. Lett.*, 2000, **68**, 229–234.
- 56 Y. Takita, M. Ninomiya, R. Matsuzaki, H. Wakamatsu, H. Nishiguchi and T. Ishihara, *Phys. Chem. Chem. Phys.*, 1999, **1**, 2367–2372.
- 57 B. Gallace and J. B. Moffat, *J. Catal.*, 1982, **76**, 182.
- 58 F. Pazoki, S. Bagheri, M. Shamsayei, M. J. Nejad and A. Heydari, *Mater. Chem. Phys.*, 2020, **253**, 123327.
- 59 T. Aihara, W. Aoki, S. Kiyohara, Y. Kumagai, K. Kamata and M. Hara, *ACS Appl. Mater. Interfaces*, 2023, **15**, 17957–17968.
- 60 M. Koutani, E. Hayashi, K. Kamata and M. Hara, *J. Am. Chem. Soc.*, 2022, **144**, 14090–14100.
- 61 Y. Yamaguchi, R. Aono, E. Hayashi, K. Kamata and M. Hara, *ACS Appl. Mater. Interfaces*, 2020, **12**, 36004–36013.
- 62 P. E. Blochl, *Phys. Rev. B: Condens. Matter Mater. Phys.*, 1994, **50**, 17953–17979.
- 63 J. Sun, A. Ruzsinszky and J. P. Perdew, *Phys. Rev. Lett.*, 2015, **115**, 036402.
- 64 G. Kresse and J. Furthmuller, *Phys. Rev. B: Condens. Matter Mater. Phys.*, 1996, **54**, 11169–11186.
- 65 G. Kresse and J. Furthmuller, *Comput. Mater. Sci.*, 1996, **6**, 15–50.
- 66 B. Romero, S. Bruque, M. A. G. Aranda and J. E. Iglesias, *Inorg. Chem.*, 2002, **33**, 1869–1874.
- 67 K. Takanabe and E. Iglesia, *Angew. Chem., Int. Ed.*, 2008, **47**, 7689–7693.
- 68 E. Hayashi, T. Tamura, T. Aihara, K. Kamata and M. Hara, *ACS Appl. Mater. Interfaces*, 2022, **14**, 6528–6537.
- 69 K. Sugahara, K. Kamata, S. Muratsugu and M. Hara, *ACS Omega*, 2017, **2**, 1608–1616.

- 70 S. Kawasaki, K. Kamata and M. Hara, *ChemCatChem*, 2016, **8**, 3247–3253.
- 71 V. D. Makwana, Y. C. Son, A. R. Howell and S. L. Suib, *J. Catal.*, 2002, **210**, 46–52.
- 72 P. Deng, H. Wang, R. Qi, J. Zhu, S. Chen, F. Yang, L. Zhou, K. Qi, H. Liu and B. Y. Xia, *ACS Catal.*, 2020, **10**, 743–750.
- 73 Q. Jing, L. Huang, Q. Li, Y. Song and L. Chen, *J. Mater. Sci.: Mater. Electron.*, 2020, **31**, 20954–20963.
- 74 J. Gong, C. S. Lee, E. J. Kim, J. H. Kim, W. Lee and Y. S. Chang, *ACS Appl. Mater. Interfaces*, 2017, **9**, 28426–28432.
- 75 J. Liu, S. Guo, H. Wu, X. Zhang, J. Li and K. Zhou, *J. Mater. Sci. Technol.*, 2021, **85**, 1–10.
- 76 J. Sun, J. Wen, G. Wu, Z. Zhang, X. Chen, G. Wang and M. Liu, *Adv. Funct. Mater.*, 2020, **30**, 2004108.
- 77 Q. Chen, Y. Wang and H. Wang, *J. Non-Cryst. Solids*, 2018, **481**, 85–93.
- 78 L. N. Elliott, D. Austin, R. A. Bourne, A. Hassanpour, J. Robb, J. L. Edwards, S. Sutcliffe and T. N. Hunter, *Langmuir*, 2023, **39**, 5697–5709.
- 79 T. Komanoya, K. Nakajima, M. Kitano and M. Hara, *J. Phys. Chem. C*, 2015, **119**, 26540–26546.